Journal of Materials Chemistry A

ROYAL SOCIETY OF CHEMISTRY

PAPER

View Article Online
View Journal | View Issue

Cite this: J. Mater. Chem. A, 2024, 12, 23769

Designing strategies for high-redox-potential conjugated carbonyl organic cathodes in lithium- and sodium-ion batteries†

Zhaoli Liu,[a] Xiangyu Meng,[b] Fengchao Cui*[a] and Guangshan Zhu *[a]

Conjugated carbonyl compounds are promising cathode materials in lithium- and sodium-ion batteries due to their high structural diversity, specific capacity and fast reaction kinetics. However, these materials are plagued by low discharge potentials and high solubility, which hinder their practical application in battery systems. To address these challenges, molecular design strategies have been proposed, including the introduction of fully unsaturated five-membered rings, the adjustment of carbonyl group position and the substitution of functional groups. The results show that placing carbonyls on the rings with stronger aromaticity of the conjugated skeleton and incorporating fully unsaturated five-membered rings into the conjugated skeleton of carbonyl compounds are favorable approaches for generating molecules with higher redox potentials. Six-designed carbonyl electrodes, CAT, CAT-CN, AST, BST, BST-CN and PST, exhibit outstanding adiabatic redox potential in the range of 3.18–4.61 V *vs.* Li/Li^+ and 2.84–4.44 V *vs.* Na/Na^+. We have conducted in-depth investigations to uncover the intrinsic factors that enhance their redox potentials, as well as the underlying mechanism of lithium/sodium storage during the discharging process. Furthermore, our predictions indicate that CAT-CN and CAT possess higher theoretical specific capacity and energy density compared to conventional inorganic and organic materials. The solubility analysis suggests that anchoring these carbonyl compounds onto conductive carbon materials, such as graphene, can effectively mitigate their solubility in electrolytes. This work provides valuable insights into designing high-performance organic cathodes for lithium- and sodium-ion batteries.

Received 1st June 2024
Accepted 22nd July 2024

DOI: 10.1039/d4ta03793f

rsc.li/materials-a

Introduction

Currently, electricity generation is dominated by non-renewable energy sources, such as fossil fuels, which are responsible for environmental pollution and global warming.[1] To phase out fossil fuel power generation and facilitate the transition to renewable energy sources, the development of energy storage systems has become crucial to balance electricity generation from intermittent renewable sources and real-time demand. In the last two decades, the development of battery energy storage has seen a significant explosion. Lithium-ion batteries (LIBs) play a pivotal role in this growth. For example, battery energy storage in the US has steadily increased, hitting 1000 MW h in 2018, with 91% attributed to LIBs.[2] Due to their excellent energy density and cycle life, LIBs are the primary energy storage devices for portable electronics such as electric vehicles, mobile phones, and laptops. However, with limited sources of lithium around the world (~0.0065% in the crust of the earth), LIBs may not be suitable for grid-scale energy storage in the long term.[3] In this context, sodium-ion batteries (SIBs) have emerged as a promising alternative, as sodium is not only much more abundant in the crust of the earth (~2.74%) compared to lithium but also Na and Li exhibit similar chemical properties.[3]

In the past, the cathodes of LIBs are typically made of transition metal oxides (*e.g.*, $LiCoO_2$ (LCO), $LiMn_2O_4$ (LMO), $LiNi_{1/3}Co_{1/3}Mn_{1/3}$, and $LiFePO_4$ (LFP)). However, these materials are unsustainable, environmentally harmful, and possess sluggish ionic diffusivity.[4] In this context, organic electrode materials have emerged as attractive alternatives due to their low carbon footprint, sustainable production, and flexible adjustable structure. These organic materials can be used for a variety of metal ion batteries, including Li^+, Na^+ and K^+ systems.[5] Among various organic electrode materials, conjugated carbonyl compounds have garnered significant interest due to their

[a]Key Laboratory of Polyoxometalate and Reticular Material Chemistry of Ministry of Education, Faculty of Chemistry, Northeast Normal University, 5268 Renmin Street, Changchun, 130024, P. R. China. E-mail: cuifc705@nenu.edu.cn; zhugs@nenu.edu.cn
[b]Jilin Vocational College of Industry and Technology, Jilin 132000, P. R. China

† Electronic supplementary information (ESI) available: The aromaticity of the designed derivatives was evaluated; the binding mechanisms between representative derivatives with Na during the discharging process; the curves that charge capacity and density energy vary with adiabatic redox potentials during the discharging process; contributions of solvation energy and electron affinity on adiabatic redox properties; contributions of charging and reorganization energies on adiabatic redox properties; the optimal configurations of cathode–graphene dimers; the comparisons between our calculated redox potentials for the reported compounds and their experimental values. See DOI: https://doi.org/10.1039/d4ta03793f

superior properties, including high specific capacity, fast redox kinetics and high power density.[6–8] However, these organic carbonyl materials fall short of meeting the cathodic demand for commercialization due to their intrinsic lower working potential (2–3 V *vs.* Li/Li^+), which is incomparable to the state-of-the-art inorganic electrode materials (3–4 V *vs.* Li/Li^+).[6,7] Tailoring the electronic structures of organic carbonyl materials through appropriate strategies could enhance their redox potential (RP).

So far, researchers have explored various strategies to enhance the RP of conjugated carbonyl materials. For example, Zhu's group incorporated boron and pyridine-type nitrogen into two conjugated carbonyl compounds, namely $(t\text{-Bu})_3$TOT and (Br_3TOT), demonstrating that both two-boron- or pyridine-type nitrogen-doped strategies are beneficial for improving the adiabatic redox potentials (ARP) when compared with the pristine $(t\text{-Bu})_3$TOT and Br_3TOT.[9] Chen *et al.* found that the RP of quinone isomers follows this order: *para*-quinones < discrete-quinones < *ortho*-quinones.[10] Jang *et al.* observed that the ARP of a series of quinone derivatives decreases with increasing the aromaticity of the backbone, and introducing electron-withdrawing functional groups can further increase the ARP.[11] Jung *et al.* incorporated carbonyl groups into the hexagon ring of pristine sumanene in various numbers and acquired a series of carbonyl derivatives with high ARP of 2.7–3.7 (V *vs.* Li/Li^+).[12] Kim *et al.* emphasized that quinones with conjugating backbones exhibit higher ARP for longer backbones, due to the strengthened inductive effect.[13] Jeong *et al.* introduced four cyano function groups into 1,4-benzoquinone, furnishing remarkably high ARP (4.50 V *vs.* Li/Li^+), charge capacity and energy density (515 mA h g^{-1} and 1517 mW h g^{-1}).[14] Despite these discoveries, there are still ample opportunities to explore new strategies for increasing the RP of carbonyl cathodes, which could enable the development of high-performance organic cathode materials for energy storage applications.

Recently, 4,5,9,10-tetracarbonyl-pyrenetetrone (PTO) has been widely used as a building block for electrode materials owing to its high density of active functional groups (carbonyl) and conjugated backbone.[15–17] Building upon this foundation, the current work has developed five promising strategies to modify the structure of PTO, generating several pyrenetetrone derivatives (CAT, CAP, CAT-CN, CAT-NH_2, AST, BST, BST-CN, BST-NH_2 and PST) as shown in Fig. 1. Density functional theory (DFT) calculation has predicted that several of these derivatives, including CAT, CAT-CN, AST, BST, BST-CN and PST, exhibit excellent open-circuit voltage (3.18–4.61 V *vs.* Li/Li^+), making them suitable candidates for cathode materials in LIBs and SIBs. Subsequent investigations were undertaken to elucidate the lithium/sodium insertion mechanism and to assess the changes in ARP upon lithiation/sodiation during the discharging process. The study also evaluated critical electrode performance parameters, such as charge capacity and energy density for these derivatives. Furthermore, an analysis was conducted to identify the key factors influencing the ARP of derivatives with or without lithium insertion. Finally, the insolubility of these derivatives, both with and without bound graphene, was estimated by a simple computational protocol. This methodological approach is anticipated to contribute significantly to the development of high-potential carbonyl-based cathode materials for advanced LIBs and SIBs.

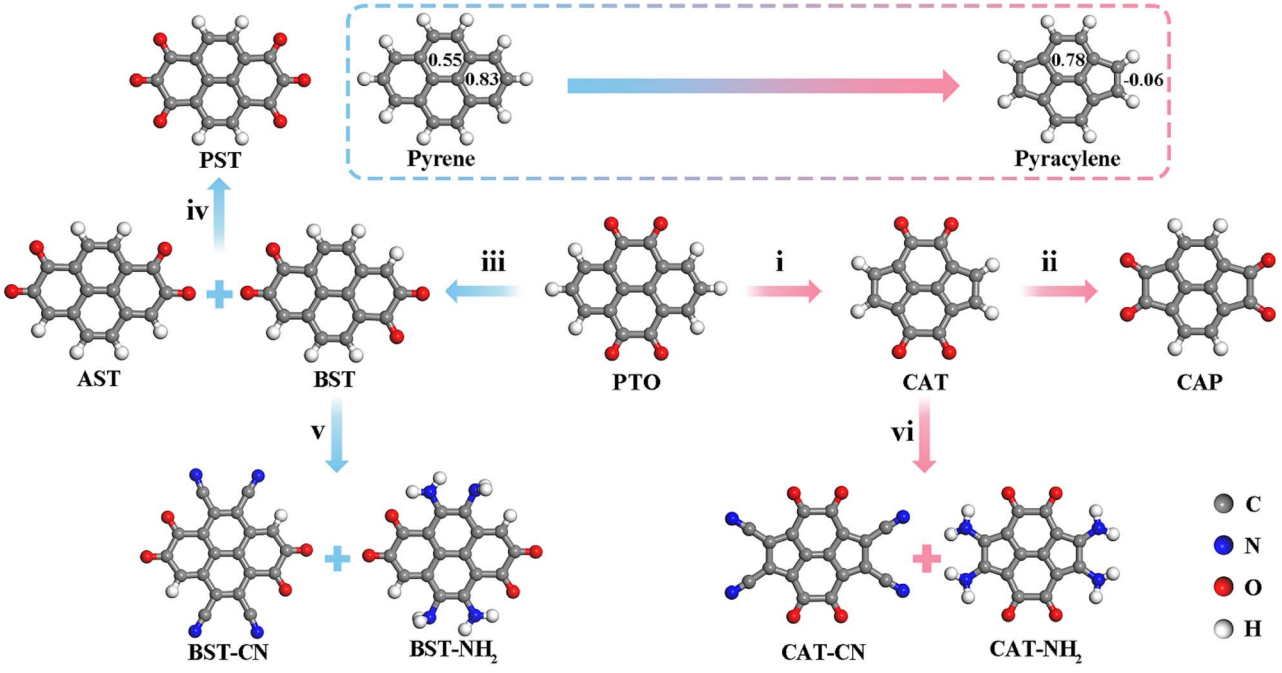

Fig. 1 Chemical structures of pyrene, pyracylene, 4,5,9,10-pyrenetetrone (PTO) and other pyrenetetrone derivatives designed by us. The values depict the HOMA of corresponding rings in pyrene and pyracylene. The atoms with grey, white, red and blue in color depict carbon, hydrogen, oxygen and nitrogen respectively.

Computational method

All geometry optimization was performed at Perdew–Burke–Ernzerhof hybrid functional (PBE0)[18]/6-31+G(d,p)[19–27] level in Gaussian 16 software.[28] The SMD[29] model was employed to calculate the thermodynamic energy of the compounds in the electrolyte (1 M $LiPF_6$ in dimethyl carbonate (DMC) and ethylene carbonate (EC) (7 : 3, v/v)) with a dielectric constant of 16.14.

The ARP (ΔE_{red}) of organic compounds without or with bound Li/Na atoms, *versus* the Li/Li^+ (Na/Na^+) electrode, were reliably calculated by

$$\Delta E_{red} = -\Delta G_{red}(sol)/nF - E_{M/M^+} \quad (1)$$

Here, $\Delta G_{red}(sol)$ denotes the change in the Gibbs free energy of the reduction process in solution,[30,31] n is the number of electrons transferred during the reduction process and F is Faraday constant. E_{M/M^+} is the RP of the Li/Li^+ and Na/Na^+ reference electrode, values are 1.39 V and 1.73 V, respectively.

The accuracy of the computational methods had been validated in the previous reports[9] and was listed in Table S1.† The differences between the calculated ARP and the values from experiments are lower than 0.36 V.

The specific charge capacity (Q, mA h g^{-1}) was computed by

$$Q = nF/3.6M \quad (2)$$

where M denotes the molecular weight. The specific energy density (W, mW h g^{-1}) was calculated by

$$W = \int_0^Q V(q)\,dq \quad (3)$$

where V depicts the ARP.

The process of gaining an electron for a molecule involves two changes in thermodynamic energy: charging energy and reorganization energy. The change in thermodynamic energy resulting from the gain of an electron by a molecule without any modification to its structure is defined as charging energy. The structure relaxation of a molecule after adding an electron would cause an energy change named recombination energy.

Electrostatic potential isosurface maps (ESP)[32] and nucleus-independent chemical shift (NICS-2D) scan plane maps were acquired by Multiwfn 3.8 (ref. 33) and VMD 1.9.3.[34] The values of harmonic oscillator measure of aromaticity (HOMA), Bond Polarity Index (BPI) were acquired by Multiwfn 3.8.

The difference in HOMA of carbonyl compounds between the fully charged states and the fully discharged states, ΔHOMA, which was calculated as follows:

$$\Delta HOMA = \sum_i^n HOMA_i^L - \sum_i^n HOMA_i$$

where $HOMA_i^L$ is the HOMA value for the i-th six/five-membered ring (6/5-MR) in a lithiated carbonyl compounds, an $HOMA_i$ is the HOMA value for the i-th 6/5-MR in the carbonyl compounds.

The solubility of pyrenetetrone derivatives in a variety of organic solvents involving EC, DMC, diethyl carbonate (DEC), dioxolane (DOL), ethyl methyl carbonate (EMC), propylene carbonate (PC), and ethylene glycol dimethyl ether (DME) was estimated by the difference in binding energy (E_d) between the solvent–cathode and cathode–cathode dimers.[35] The solubility of an organic molecule in a solvent can be qualitatively analyzed based on the E_d value. E_d was calculated by the following equation:

$$E_d = E_{cs} - E_{cc} \quad (4)$$

where, E_{cs} represents the binding energy between the cathode molecule and solvent molecule, while E_{cc} denotes the binding energy between two cathode molecules. The higher the E_d value, the poorer the solubility of an organic molecule in a solvent. ABCluster software was used to search the optimal binding configurations of each dimer structure (cathode–cathode, solvent–cathode and cathode–graphene).[36,37] Subsequently, the optimal configuration was optimized at B3LYP-D3 (ref. 38 and 39)/6-311+G(d,p)[19,21,23,40–42] level. The modeling of cathode–graphene dimer structures was shown in Fig. S10† where graphene was simplified as a fragment.

Results and discussion

Strategies for designing the derivatives of pyrenetetrone

In order to gain high-potential electrode molecules, five strategies were applied to tailor the molecular structure of PTO and their derivatives: (i) the fusion of fully unsaturated five-membered rings into the sp^2-carbon framework of PTO, generating CAT molecule; (ii) altering the position of the carbonyl group in the CAT molecule, forming CAP molecule; (iii) changing the location of the carbonyl groups in PTO, building AST and BST molecule; (iv) increase the concentration of carbonyl groups in AST and BST, acquiring PST; (v) the displacement of two types of functional groups on BST and CAT, $–NH_2$ (with electron-donating nature) or –CN (with electron-withdrawing nature), generating BST-NH_2, BST-CN, CAT-NH_2 and CAT-CN molecules. A total of nine derivatives of PTO were designed relying on the above strategies (shown in Fig. 1).

ARP of pyrenetetrone derivatives in the fully charged states

The intrinsic redox activity of each compound determines its open-circuit RP in the fully charged state, which affects the voltage of rechargeable batteries. And, the energy density of rechargeable batteries is also dependent on their voltage. Therefore, the open-circuit RP could be used to assess the viability of materials as organic cathodes. A reliable computational method was used to calculate the ARP of the designed derivatives, as shown in Table 1. The open-circuit RP of pyrenetetrone derivatives ranged from 2.08 to 4.61 V *versus* Li/Li^+, in their fully charged states. Notably, the open-circuit RP of the derivatives including CAT, CAT-CN, CAP, AST, BST, BST-CN and PST, were significantly improved compared to the parent compound PTO. The decisive factors were revealed to tune the open-circuit RP of these pyrenetetrone derivatives:

(i) The introduction of fully unsaturated five-membered rings in CAT resulted in a more negative BPI of carbonyl

Table 1 The HOMA, BPI and ARP for pyrene, pyracylene, 4,5,9,10-pyrenetetrone (PTO) and other pyrenetetrone derivatives designed by us

Molecule	HOMA[a]	HOMA[b]	BPI	ARP (V *vs.* Li/Li^+)	ARP (V *vs.* Na/Na^+)
Pyrene	0.83	0.55			
Pyracylene	0.78	−0.06			
PTO	0.96	−1.08	−0.14	2.62	2.29
CAT	0.39	−1.89	−0.15	3.54	3.20
CAP	0.91	−2.32	−0.14	2.83	2.49
AST	0.91/−0.03	−1.20	−0.17/−0.12	3.18	2.84
BST	0.32	−0.99	−0.17/−0.12	3.89	3.55
PST	0.78	−1.94	−0.13/−0.13	3.34	3.00
CAT-CN	0.96	−1.11	−0.16	4.61	4.44
CAT-NH_2	0.43	−1.47	−0.11	2.08	1.74
BST-CN	0.25	−0.94	−0.19/−0.14	4.54	4.20
BST-NH_2	0.14	−0.84	−0.15/−0.05	3.78	3.44

[a] HOMA of the single benzene rings without carbonyl groups. [b] HOMA of the single benzene rings with carbonyl groups.

groups (the active functional groups) compared to PTO (a more negative BPI indicates a greater tendency to accept electrons during the discharge process, leading to a higher ARP (3.54 V *vs.* Li/Li^+)). To clarify the underlying causes, we calculated the HOMA and NICS-2D scan plane map of pyracylene and pyrene, depicted in Fig. 1 and S2.† The six-membered rings of pyrene and pyracylene exhibit positive HOMA values, indicating their aromaticity, while the five-membered rings of pyracylene have negative HOMA values, indicating their anti-aromaticity. Furthermore, NICS-2D scan plane maps demonstrate that the fully unsaturated five-membered rings in pyracylene have stronger anti-aromaticity while the six-membered rings have weaker aromaticity. Thus, fully unsaturated five-membered rings tend to capture electrons to satisfy Hückel's rule and gain aromaticity.[43] It can be inferred that the presence of fully unsaturated five-membered rings in CAT has an induced effect (electron absorption) on carbonyl groups, leading to its more negative BPI.

(ii) Locating the carbonyl groups on the five-membered rings of pyracylene, as in the case of CAP, resulted in a lower ARP (2.83 V *vs.* Li/Li^+) in comparison to CAT. Introducing carbonyls on the anti-aromatic five-membered rings of pyracylene would disrupt their anti-aromaticity, partially increasing the BPI and decreasing the ARP of CAP compared to CAT. These results suggest that placing carbonyl groups onto aromatic rings is more effective in increasing the ARP of the conjugated skeleton than on anti-aromatic rings.

(iii) BST (3.89 V *vs.* Li/Li^+) and AST (3.18 V *vs.* Li/Li^+) exhibit higher ARP than PTO (2.62 V *vs.* Li/Li^+), similar to the case of CAT and CAP. Pyrene has two types of six-membered rings with different HOMA values: 0.55 and 0.83. Introducing carbonyls into the rings with higher HOMA values (more aromatic) would generate AST and BST with lower BPI of carbonyls, resulting in higher ARP than PTO, where the carbonyls are located in the less aromatic rings. In general, placing carbonyl groups on the more aromatic rings of a conjugated skeleton leads to derivatives with higher ARP. Surprisingly, the ARP of BST is much higher than that of AST, which would be attributed to the difference in aromaticity for their conjugated backbones. As shown in Fig. S2,† the aromaticity of AST is stronger than that of BST. Stronger aromaticity makes it more difficult to accept electrons for AST, leading to weaker oxidation properties and lower ARP.

(iv) The ARP of PST (3.34 V *vs.* Li/Li^+) is higher than that of AST but lower than BST, demonstrating that the amount and location of carbonyl groups synergistically influence the ARP. As shown in Fig. S1,† the stronger aromaticity of the AB ring in the PST skeleton results in a higher minimum BPI of the carbonyl, causing a lower ARP compared to BST.

(v) The –CN and $–NH_2$, exhibiting prominent electron withdrawing/donating nature and lower molecular weight among common functional groups, were preferentially selected to modulate the redox properties of BST and CAT. Compared to unsubstituted analogs, the ARP of electron-withdrawing and electron-donating substituted derivatives are significantly increased and reduced, respectively (Table 1). It is worth noting that the minimum BPI of the carbonyls in the analogs substituted by –CN and substituted by $–NH_2$ decrease and increase compared to that of unsubstituted counterparts, respectively. The data indicate that the –CN group, with its strong electron-withdrawing effect, increases the polarity of carbonyl groups, enhancing the redox potential of the derivative. Conversely, the $–NH_2$ group, being a strong electron donor, reduces the polarity of carbonyl groups, thereby reducing their redox potentials.

Furthermore, we carried out a detailed analysis of the ARP for CAT modified with various electron-donating groups (–OH, $–OCH_3$) and electron-withdrawing groups (–F, –Cl, –Br, $–CF_3$) (Fig. S3†). The higher ARP values of CAT-F, CAT-Cl, CAT-Br, and CAT-CF_3, and the lower ARP values of CAT-OCH_3 and CAP-OH than CAT, support our conclusion that the ARP of electron-withdrawing and electron-donating substituted derivatives are increased and decreased, respectively.

Mechanism of lithium/sodium storage during the discharging process

The open-circuited ARP of the fully charged derivatives discussed above provide insights for designing materials that favor

reduction. Besides, it should be emphasized that the cathode materials would insert the Li during the discharging processes. Therefore, it is necessary to investigate the binding mechanism between the materials and Li to understand the alteration in ARP of the electrode materials during the discharging process.

Based on the Li atoms with gradually increased numbers interacting with the derivatives to form the most stable composite configurations, the binding status of Li atoms with the representative compounds (CAT, CAP CAT-CN, AST, BST, BST-CN, and PST) during the discharging process is depicted in Fig. 2a. For the seven compounds, the first and second Li atoms tend to be located in the middle of the *ortho*-carbonyl groups owing to the strong chelation between the carbonyls. It also can be rationalized by the most negative electrostatic potential in the ESP isosurface maps of the bare derivatives. Subsequently, the third and fourth Li also bind in the middle of *ortho*-carbonyls for CAT, CAP, AST, BST and PST. Interestingly, for the CAT-CN and BST-CN, the third and fourth Li are prone to locate between the cyano groups. This suggests that the introduction of the cyano groups not only favors the improvement of ARP but also the Li-storage capacity.

The changes in the ARP for the seven pyrenetetrone derivatives with the increasing binding Li atoms are evaluated in Fig. 2a. The ARP decrease as the Li atoms increase, due to the receding of their oxidability induced by the incorporation of Li atoms. This continuous decrease of their oxidability will eventually lead to a negative (or approached zero) ARP and thus to cathodic deactivation, which guides us to quantify the Li-

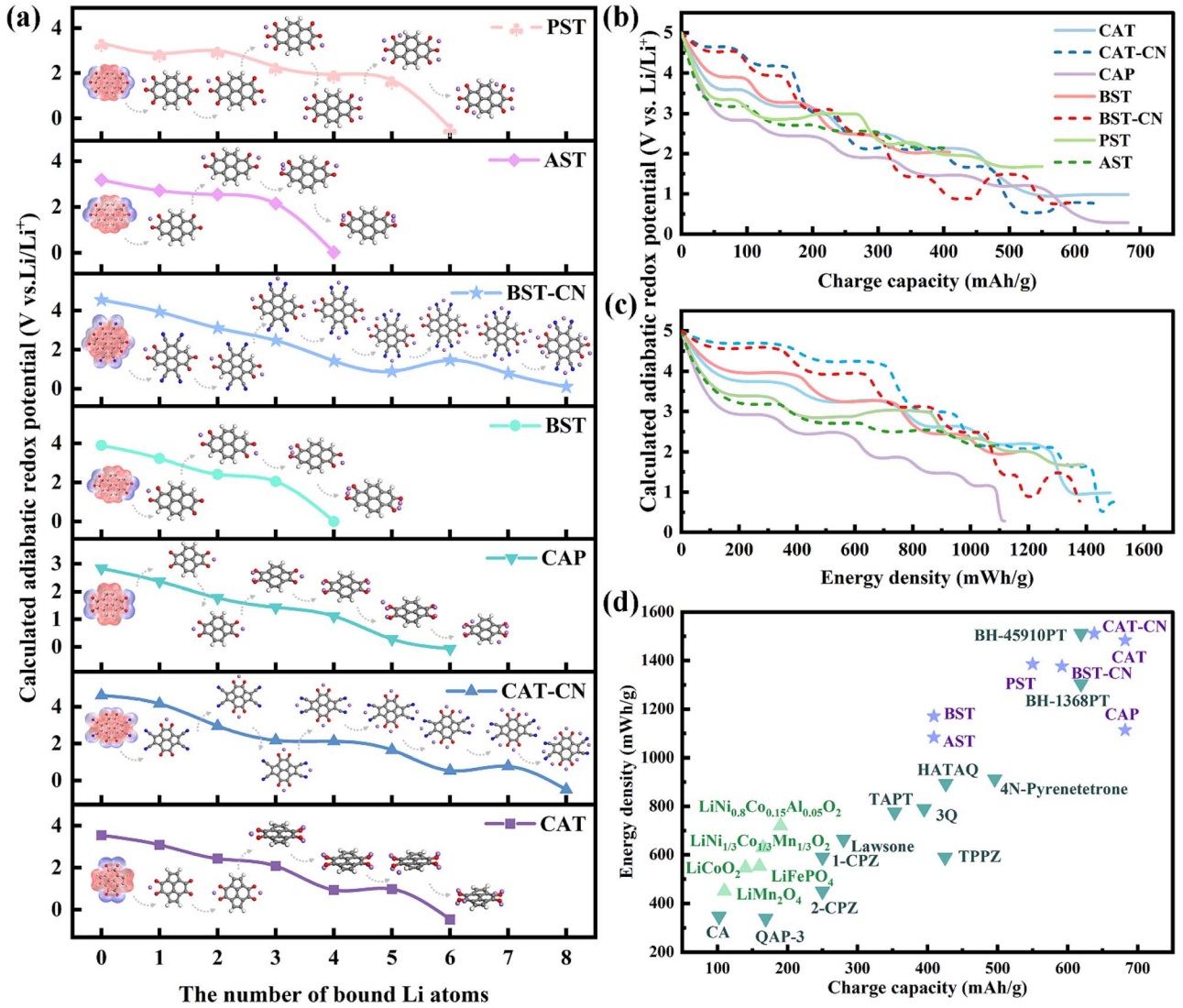

Fig. 2 The evolution of derivatives in the discharging process and their electrochemical performances. (a) The Li-ion storage sites and the structural evolution for seven pyrenetetrone derivatives (CAT, CAT-CN, CAP, BST, BST-CN, AST, and PST) and their variety of ARP as a function of the number of bound Li atoms. The atoms with grey, white, red, blue and purple depict carbon, hydrogen, oxygen, nitrogen and lithium, respectively. (b) Resultant profiles of the gravimetric charge capacities and (c) energy densities as a function of ARP. (d) The Ragone plot shows the performance parameters of the pyrenetetrone derivatives reported by this work, the conventional inorganic compounds[43,44] and the outstanding organic compounds[35,46–50] referred from previous studies.

storage capacity of a compound. According to Fig. 2a, CAT, CAT-CN, CAP, BST, BST-CN, AST and PST exhibit the theoretical Li-storage capacities of 6, 8, 6, 4, 8, 4 and 6, respectively. Notably, the Li-storage capacities of BST are lower than those of CAT and CAP, although they share the same number of activity groups, carbonyl. This reveals that molecules with the same amount of activity groups do not necessarily store the same number of lithium atoms, suggesting that quantifying the Li storage capacity solely based on the activity groups may be inappropriate in some cases.

Following, to verify the thermodynamic stability of carbonyl compounds upon Li insertion, we further calculated the difference of their HOMA between the fully charged states and the fully discharged states, ΔHOMA. A positive value of ΔHOMA means an increase in aromaticity, resulting in that the structure becomes more stable in thermodynamically upon Li insertion. Fig. S4† shows that CAT, CAT-CN, CAP, BST, BST-CN, AST and PST all exhibits positive ΔHOMA in the fully discharged state indicating that they are thermodynamically stable after Li insertion.

Based on corresponding process of lithiation discussed above, the voltage–performance curves of seven derivatives calculated by eqn (2) and (3) are plotted in Fig. 2b and c. The performance parameters (*vs.* Li/Li^+), including gravimetric charge capacity and energy density of these derivatives, are in the range of 409–682 mA h g^{-1} and 1083–1511 mW h g^{-1}, respectively, as listed in Table 2. Among these derivatives, CAT-CN and BST-CN show the highest Li-storage numbers, while lower theoretical charge capacities (638 and 592 mA h g^{-1}) compared to CAT (682 mA h g^{-1}) and CAP (682 mA h g^{-1}), due to their higher molecular weights. On the other hand, the gravimetric energy density of CAT (1483 mW h g^{-1}) and CAP (1113 mW h g^{-1}) is lower than that of CAT-CN (1511 mW h g^{-1}), as both the charge capacity and the ARP contribute cooperatively to the energy density. During the discharging process, CAT-CN sustains higher ARP than CAT and CAP, resulting in a higher energy density. Fig. 2d shows the Ragone plot that summarizes the performance of the seven pyrenetetrone derivatives, conventional inorganic materials[44,45] and newly developed organic materials[35,46–50] as cathodes of LIBs. It can be observed that the CAT-CN and CAT present visible advantages compared to other materials.

Further, the performance parameters of these derivatives as cathodes of SIBs were also assessed. Fig. S5† shows the decrease of the ARP for the seven pyrenetetrone derivatives with the increasing number of bound Na atoms during the discharging process. Except for BST, similar positions are occupied for storing Li and Na atoms in the same derivatives. In addition, the derivatives including CAT, CAT-CN, CAP and BST-CN, store Na atoms with numbers of 5, 7, 5 and 7 respectively, which are lower than their Li-storage capacity. BST has a higher Na storage capacity of 5 than Li. AST and PST have the same storage capacity of Li and Na atoms. These results suggest that the capacity of a cathode may differ for the various storage metal ions. Fig. S6† shows the voltage–performance curves of the seven derivatives based on the Na storage process described above. CAT and CAP exhibit the highest charge capacity of 567 mA h g^{-1}, while CAT-CN has the highest energy density of 1188 mW h g^{-1}, as listed in Table 2. The performance of the seven pyrenetetrone derivatives as cathodes of SIBs was summarized in the Ragone plot shown in Fig. S6.† It can be observed that CAT-CN exhibits higher charge capacity and energy density compared to the conventional inorganic [51–58] and organic materials.[59–66]

Key factors affecting redox properties of pyrenetetrone derivatives

As known to all, the redox property of an organic molecule relies acutely on the electronic structure involving the lowest unoccupied molecular orbital (LUMO), highest occupied molecular orbital (HOMO), and electron affinity (EA) denoting the change of the Gibbs free energy after capturing an electron. Fig. 3 shows the correlations between ARP and EA, HOMO, LUMO and HOMO–LUMO gap, with the Pearson correlation coefficients (r) of −0.93, −0.86, −0.97 and 0.082, respectively. This verified that both EA and LUMO are strongly linearly correlated with ARP. In essence, molecules with more negative LUMO and EA exhibit higher ARP owing to improved oxidative activity. The linear correlations provide an efficient method to estimate the ARP of a molecule by the EA or LUMO, thereby conserving computational resources.

However, this linear relationship weakens as the ARP approaches negative values, where the continuous degradation of the oxidative ability during the discharging process leads to

Table 2 The gravimetric charge capacities and energy densities of seven pyrenetetrone derivatives (CAT-CN, CAT, PST, BST-CN, BST, AST and CAP) as cathodes in LIBs and NIBs

	LIBs		NIBs	
Molecule	Charge capacity (mA h g^{-1})	Energy density (mW h g^{-1})	Charge capacity (mA h g^{-1})	Energy density (mW h g^{-1})
CAT-CN	638	1511	565	1188
CAT	682	1483	567	1070
PST	550	1385	550	1071
BST-CN	592	1376	518	989
BST	409	1183	511	1002
AST	409	1083	409	881
CAP	682	1113	567	763

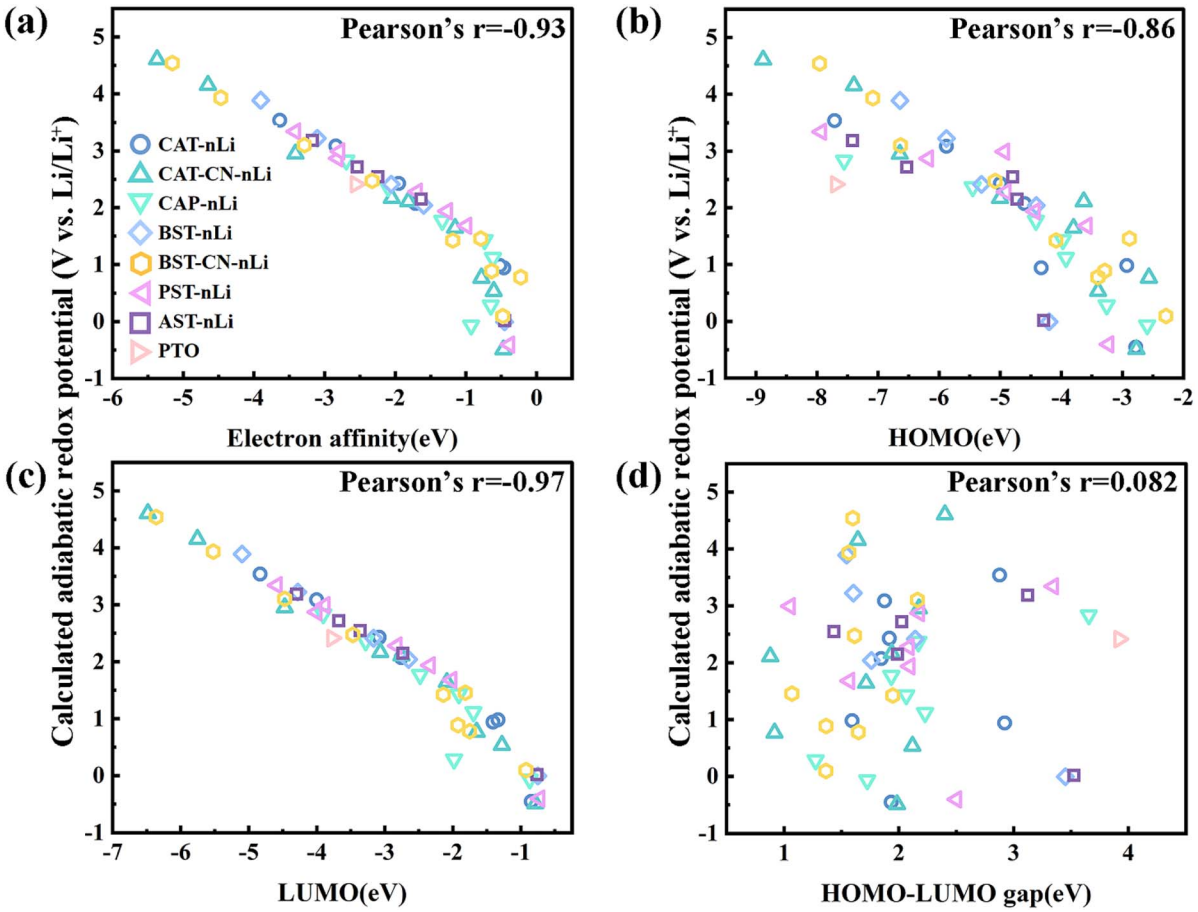

Fig. 3 The correlations of ARP with (a) electron affinity (EA), (b) HOMO, (c) LUMO and (d) HOMO–LUMO gap.

the ARP becoming negative. Thus, the change in the ARP is determined not only by the electronic properties but also by other factors. Generally, the solvent environment in the electrolyte generates the solvation thermodynamics that affect the ARP. To evaluate this effect, we calculated the solvation energy (E_s) on the ARP (the change in the solvation free energy of a cluster model is called E_s). Fig. S7 and S8† illustrate the contributions of EA and E_s to the ARP.

As shown in Fig. S7 and S8,† the sum of the EA and E_s is negatively correlated with the ARP. When the ARP exceeds 2.0 V, E_s is higher than EA, indicating that the EA dominates the ARP; below 2.0 V, EA rises and exceeds E_s, where E_s plays a non-negligible role. Briefly, increasing EA is dominant for the continuous decrease of the ARP above 2.0 V, while both E_s and EA are synergistically responsible for the decrease of the ARP below 2.0 V. This indicates that the ARP is affected by both EA and E_s, explaining the deviation from linearity in the correlation between the ARP and the EA.

To gain deep insight into the electrochemical properties of the pyrenetetrone derivatives, EA was decomposed into the charging and reorganization energy. Fig. S9† indicates that the charging and reorganization energies contribute synergistically to the ARP. The reorganization energy remains a puny negative value for different compounds, indicating that the ARP is primarily determined by the charging energy. The increase in charging energy leads to the decrease in ARP. The tiny negative reorganization energy also indicates that the structures of these derivatives are adequately stable, even after attaching Li atoms.

Solubility of the pyrenetetrone derivatives

In general, electrodes made of small organic molecules have a tendency to dissolve in the electrolyte, which would reduce the cycle life of LIBs. Therefore, identifying the solubility of pyrenetetrone derivatives is crucial to assessing their feasibility as cathodes. A descriptor, the difference of binding energy (E_d) between the cathode–solvent and cathode–cathode dimers, was introduced to describe the solubility of organic molecules.[35] Fig. 4a shows the E_d of the pyrenetetrone derivatives in several organic solvents. Among these derivatives, BST has the lowest solubility in the seven electrolyte solvents due to the highest E_d value (>7 kcal mol^{-1}). It can be observed that increased carbonyl concentration and the introduction of cyano groups in compounds lead to a higher solubility, as evidenced by CAT-CN and PST having poorer insolubility with a smaller E_d for some solvents. In addition, the E_d of a compound may differ in different solvents, *e.g.* CAT-CN tends to dissolve in the PC while not dissolving in DOL, indicating that E_d can provide a criterion for choosing proper electrolytes for the cathodes. To mitigate the dissolution of derivatives, they can be bound onto

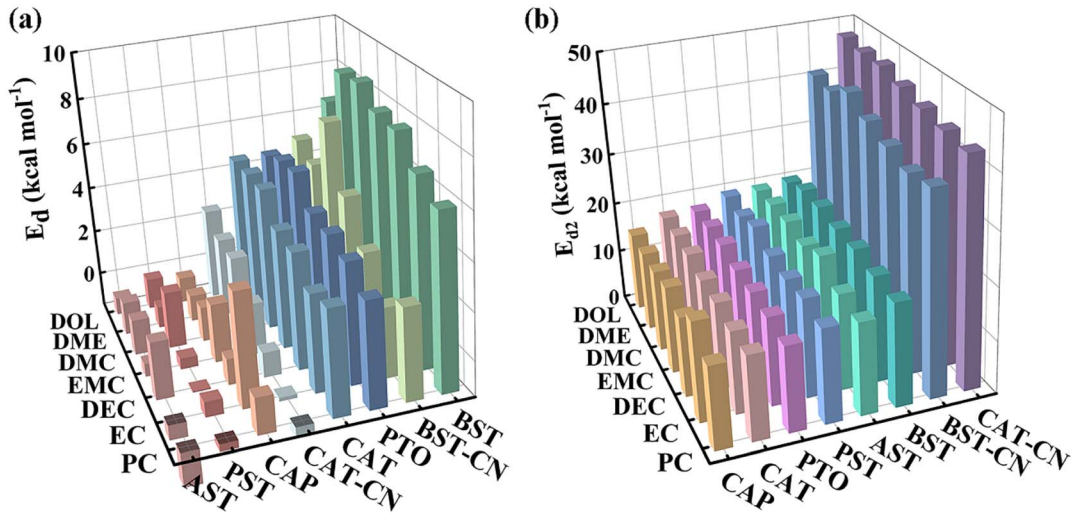

Fig. 4 (a) The differences in binding energy (E_d) between cathode–cathode and cathode–solvent complexes. (b) The differences in binding energy (E_{d2}) between cathode–graphene and cathode–solvent complexes.

conductive carbon materials, such as graphene. Thus, we calculated the difference in binding energy between the cathode–graphene and cathode–solvent (E_{d2}) to measure the solubility after the organic molecules bond with graphene, as depicted in Fig. 4b. Comparing Fig. 4a and b, a notable decrease in solubility among pyrenetetrone derivatives is observed, with CAT-CN exhibiting the lowest solubility due to its highest E_{d2} value (>40 kcal mol^{-1}).

Conclusions

In this work, we have designed a series of pyrenetetrone derivatives, namely CAT, CAP, CAT-CN, PST, AST, BST and BST-CN, which are considered as potential cathode materials for LIBs and SIBs. A comprehensive computational investigation was conducted to study their redox properties in the fully charged state and during the discharging processes. Several key findings emerge from this study. The designed CAT exhibits a higher open-circuit potential of 3.54 V *vs.* Li/Li$^+$, indicating that incorporating fully unsaturated five-membered rings into sp^2-carbon frameworks of carbonyl compounds is an efficient strategy to enhance their ARP. Secondly, placing the carbonyl groups on the rings with stronger aromaticity, such as the six-membered ring of pyracylene in CAT (HOMA = 0.78) leading to a higher ARP compared to the five-membered ring (HOMA = −0.06). Thirdly, the insertion of two carbonyls in BST to produce PST results in a lower ARP of 3.32 V *vs.* Li/Li$^+$ than that of BST, due to the stronger aromaticity in the conjugated skeleton, indicating that the greater aromaticity for a conjugated carbonyl compound may be detrimental to the improvement of the ARP. Fourthly, substituting four electron-withdrawing cyano groups (–CN) in BST and CAT yields BST-CN and CAT-CN with significantly heightened ARP of 4.54 and 4.61 V *vs.* Li/Li$^+$, respectively, exceeding most organic and inorganic cathode materials. Examining the redox behavior during the discharge process reveals that all derivatives bind Li and Na atoms near the cyano or carbonyl group. Among them, BST-CN and CAT-CN display the highest lithium- and sodium-capacities. Based on this, we further quantified their theoretical charge capacity and energy density. As LIB cathodes, CAT offers the highest charge capacity (682 mA h g^{-1}, 1483 mW h g^{-1}), while CAT-CN presents the highest energy density (638 mA h g^{-1}, 1511 mW h g^{-1}). For SIB cathodes, CAT exhibits the highest charge capacity (567 mA h g^{-1}, 1070 mW h g^{-1}) and CAT-CN has the highest energy density (565 mA h g^{-1}, 1188 mW h g^{-1}). Finally, a simplified computational protocol was used to characterize the solubility of these derivatives in the electrolyte. While the introduction of cyano and carbonyl groups in derivatives increases the solubility, running counter to the other performance metrics, such as charge capacity. This issue can be addressed by binding with the conduct carbon materials. In conclusion, this study provides insights into designing high-performance organic carbonyl cathode materials for LIBs and SIBs, highlighting strategies to enhance RP and mitigate solubility.

Data availability

Data supporting this article have been included as part of the ESI.†

Author contributions

Zhaoli Liu: conceptualization, data curation, formal analysis, investigation and writing – original draft; Xiangyu Meng: software, supervision and resources; Fengchao Cui: writing – review & editing, validation, funding acquisition and project administration; Guangshan Zhu: validation, resources and supervision.

Conflicts of interest

The authors respectfully declare that there are no conflicts of interest to acknowledge for this research.

Acknowledgements

This work is financially supported by the Science & Technology Department of Jilin Province (No. 20230101023JC), the Fundamental Research Funds for the Central Universities-Excellent Youth Team Program (2412023YQ001), the National Natural Science Foundation of China (U21A20330) and the "111" Project (B18012).

References

1 Z. Zhu, T. Jiang, M. Ali, Y. Meng, Y. Jin, Y. Cui and W. Chen, Rechargeable Batteries for Grid Scale Energy Storage, *Chem. Rev.*, 2022, **122**, 16610–16751, DOI: **10.1021/acs.chemrev.2c00289**.

2 K. Mongird, V. V. Viswanathan, P. J. Balducci, M. J. Alam, V. Fotedar, V. S. Koritarov and B. Hadjerioua, *Energy Storage Technology and Cost Characterization Report*, U.S. Department of Energy (DOE), 2019.

3 J. Hu, Y. Hong, M. Guo, Y. Hu, W. Tang, S. Xu, S. Jia, B. Wei, S. Liu, C. Fan and Q. Zhang, Emerging Organic Electrodes for Na-ion and K-ion batteries, *Energy Storage Mater.*, 2023, **56**, 267–299, DOI: **10.1016/j.ensm.2023.01.021**.

4 C. N. Gannett, L. Melecio-Zambrano, M. J. Theibault, B. M. Peterson, B. P. Fors and H. D. Abruña, Organic Electrode Materials for Fast-Rate, High-Power Battery Applications, *Mater. Rep.: Energy*, 2021, **1**, 100008, DOI: **10.1016/j.matre.2021.01.003**.

5 J. J. Shea and C. Luo, Organic Electrode Materials for Metal Ion Batteries, *ACS Appl. Mater. Interfaces*, 2020, **12**, 5361–5380, DOI: **10.1021/acsami.9b20384**.

6 J. Kim, Y. Kim, J. Yoo, G. Kwon, Y. Ko and K. Kang, Organic Batteries for A Greener Rechargeable World, *Nat. Rev. Mater.*, 2022, **8**, 54–70, DOI: **10.1038/s41578-022-00478-1**.

7 Y. Lu and J. Chen, Prospects of Organic Electrode Materials for Practical Lithium Batteries, *Nat. Rev. Chem.*, 2020, **4**, 127–142, DOI: **10.1038/s41570-020-0160-9**.

8 Y. Lu, Y. Cai, Q. Zhang and J. Chen, Insights into Redox Processes and Correlated Performance of Organic Carbonyl Electrode Materials in Rechargeable Batteries, *Adv. Mater.*, 2022, **34**, 2104150, DOI: **10.1002/adma.202104150**.

9 Z. Liu, F. Cui and G. Zhu, Tailoring Electrochemical Redox Properties of Trioxotriangulene Organic Cathodes by a Heteroatom-Doped Strategy, *ACS Appl. Energy Mater.*, 2023, DOI: **10.1021/acsaem.3c01925**.

10 L. Miao, L. Liu, Z. Shang, Y. Li, Y. Lu, F. Cheng and J. Chen, The Structure-Electrochemical Property Relationship of Quinone Electrodes for Lithium-ion Batteries, *Phys. Chem. Chem. Phys.*, 2018, **20**, 13478–13484, DOI: **10.1039/C8CP00597D**.

11 K. C. Kim, T. Liu, S. W. Lee and S. S. Jang, First-Principles Density Functional Theory Modeling of Li Binding: Thermodynamics and Redox Properties of Quinone Derivatives for Lithium-Ion Batteries, *J. Am. Chem. Soc.*, 2016, **138**, 2374–2382, DOI: **10.1021/jacs.5b13279**.

12 K. H. Jung and K. C. Kim, Insights on Redox Properties of Sumanene Derivatives for High-Performance Organic Cathodes, *ACS Appl. Mater. Interfaces*, 2020, **12**, 8333–8341, DOI: **10.1021/acsami.9b21991**.

13 K. H. Jung, G. S. Jeong, C. Y. Go and K. C. Kim, Conjugacy of Organic Cathode Materials for High-potential Lithium-ion Batteries: Carbonitriles *versus* Quinones, *Energy Storage Mater.*, 2020, **24**, 237–246, DOI: **10.1016/j.ensm.2019.08.014**.

14 G. S. Jeong, D. K. Lee and K. C. Kim, Crucial Role of Cyanides for High-potential Electrochemical Reduction Reaction, *Energy Storage Mater.*, 2020, **29**, 140–148, DOI: **10.1016/j.ensm.2020.04.009**.

15 R. Shi, L. Liu, Y. Lu, Y. Li, S. Zheng, Z. Yan, K. Zhang and J. Chen, *In Situ* Polymerized Conjugated Poly(pyrene-4,5,9,10-tetraone)/Carbon Nanotubes Composites for High-Performance Cathode of Sodium Batteries, *Adv. Energy Mater.*, 2020, **11**, 2002917, DOI: **10.1002/aenm.202002917**.

16 T. Nokami, T. Matsuo, Y. Inatomi, N. Hojo, T. Tsukagoshi, H. Yoshizawa, A. Shimizu, H. Kuramoto, K. Komae, H. Tsuyama and J. Yoshida, Polymer-bound Pyrene-4,5,9,10-tetraone for Fast-charge and -discharge Lithium-ion Batteries with High Capacity, *J. Am. Chem. Soc.*, 2012, **134**, 19694–19700, DOI: **10.1021/ja306663g**.

17 S. Zheng, L. Miao, T. Sun, L. Li, T. Ma, J. Bao, Z. Tao and J. Chen, An Extended Carbonyl-rich Conjugated Polymer Cathode for High-capacity Lithium-ion Batteries, *J. Mater. Chem. A*, 2021, **9**, 2700–2705, DOI: **10.1039/D0TA11648C**.

18 M. J. Frisch, G. W. Trucks, H. B. Schlegel, G. E. Scuseria, M. A. Robb, J. R. Cheeseman, G. Scalmani, V. Barone, G. A. Petersson, H. Nakatsuji, X. Li, M. Caricato, A. V. Marenich, J. Bloino, B. G. Janesko, R. Gomperts, B. Mennucci, H. P. Hratchian, J. V. Ortiz, A. F. Izmaylov, J. L. Sonnenberg, D. Williams-Young, F. Ding, F. Lipparini, F. Egidi, J. Goings, B. Peng, A. Petrone, T. Henderson, D. Ranasinghe, V. G. Zakrzewski, J. Gao, N. Rega, G. Zheng, W. Liang, M. Hada, M. Ehara, K. Toyota, R. Fukuda, J. Hasegawa, M. Ishida, T. Nakajima, Y. Honda, O. Kitao, H. Nakai, T. Vreven, K. Throssell, J. A. Montgomery Jr, J. E. Peralta, F. Ogliaro, M. J. Bearpark, J. J. Heyd, E. N. Brothers, K. N. Kudin, V. N. Staroverov, T. A. Keith, R. Kobayashi, J. Normand, K. Raghavachari, A. P. Rendell, J. C. Burant, S. S. Iyengar, J. Tomasi, M. Cossi, J. M. Millam, M. Klene, C. Adamo, R. Cammi, J. W. Ochterski, R. L. Martin, K. Morokuma, O. Farkas, J. B. Foresman and D. J. Fox, *Gaussian 16 Revision C.01*, Gaussian Inc., Wallingford CT, 2016.

19 Y. Zhao and D. G. Truhlar, A New Local Density Functional for Main-group Thermochemistry, Transition Metal Bonding, Thermochemical Kinetics, and Noncovalent Interactions, *J. Chem. Phys.*, 2006, **125**, 194101, DOI: **10.1063/1.2370993**.

20 K. L. Schuchardt, B. T. Didier, T. Elsethagen, L. Sun, V. Gurumoorthi, J. Chase, J. Li and T. L. Windus, Basis Set Exchange: A Community Database for Computational Sciences, *J. Chem. Inf. Model.*, 2007, **47**, 1045–1052, DOI: **10.1021/ci600510j**.

21 T. Clark, J. Chandrasekhar, G. W. Spitznagel and P. V. R. Schleyer, Efficient Diffuse Function-Augmented

Basis Sets for Anion Calculations. III. The 3-21+G Basis Set for First-Row Elements, Li-F, *J. Comput. Chem.*, 1983, **4**, 294–301, DOI: 10.1002/jcc.540040303.

22 M. J. Frisch, G. W. Trucks, H. B. Schlegel, G. E. Scuseria, M. A. Robb, J. R. Cheeseman, G. Scalmani, V. Barone, B. Mennucci, G. A. Petersson, H. Nakatsuji, M. Caricato, X. Li, H. P. Hratchian, A. F. Izmaylov, J. Bloino, G. Zheng, J. L. Sonnenberg, M. Hada, M. Ehara, K. Toyota, R. Fukuda, J. Hasegawa, M. Ishida, T. Nakajima, Y. Honda, O. Kitao, H. Nakai, T. Vreven, J. A. Montgomery Jr, J. E. Peralta, F. Ogliaro, M. Bearpark, J. J. Heyd, E. Brothers, K. N. Kudin, V. N. Staroverov, R. Kobayashi, J. Normand, K. Raghavachari, A. Rendell, J. C. Burant, S. S. Iyengar, J. Tomasi, M. Cossi, N. Rega, M. J. Millam, M. Klene, J. E. Knox, J. B. Cross, V. Bakken, C. Adamo, J. Jaramillo, R. Gomperts, R. E. Stratmann, O. Yazyev, A. J. Austin, R. Cammi, C. Pomelli, J. W. Ochterski, R. L. Martin, K. Morokuma, V. G. Zakrzewski, G. A. Voth, P. Salvador, J. J. Dannenberg, S. Dapprich, A. D. Daniels, Ö. Farkas, J. B. Foresman, J. V. Ortiz, J. Cioslowski and D. J. Fox, *Gaussian 09 Revision E.01*, Gaussian Inc., Wallingford CT, 2009.

23 P. C. Hariharan and J. A. Pople, The Influence of Polarization Functions on Molecular Orbital Hydrogenation Energies, *Theor. Chim. Acta*, 1973, **28**, 213–222, DOI: 10.1007/BF00533485.

24 B. P. Pritchard, D. Altarawy, B. Didier, T. D. Gibsom and T. L. Windus, A New Basis Set Exchange: An Open, Up-to-date Resource for the Molecular Sciences Community, *J. Chem. Inf. Model.*, 2019, **59**, 4814–4820, DOI: 10.1021/acs.jcim.9b00725.

25 D. Feller, The Role of Databases in Support of Computational Chemistry Calculations, *J. Comput. Chem.*, 1996, **17**, 1571–1586, DOI: 10.1002/(SICI)1096-987X(199610)17:13<1571::AID-JCC9>3.0.CO;2-P.

26 W. J. Hehre, R. Ditchfield and J. A. Pople, Self-Consistent Molecular Orbital Methods. XII. Further Extensions of Gaussian-Type Basis Sets for Use in Molecular Orbital Studies of Organic Molecules, *J. Chem. Phys.*, 1972, **56**, 2257–2261, DOI: 10.1063/1.1677527.

27 J. D. Dill and J. A. Pople, Self-Consistent Molecular Orbital Methods. XV. Extended Gaussian-type Basis Sets for Lithium, Beryllium, and Boron, *J. Chem. Phys.*, 1975, **62**, 2921–2923, DOI: 10.1063/1.430801.

28 R. Ditchfield, W. J. Hehre and J. A. Pople, Self-Consistent Molecular-Orbital Methods. IX. An Extended Gaussian-Type Basis for Molecular-Orbital Studies of Organic Molecules, *J. Chem. Phys.*, 1971, **54**, 724–728, DOI: 10.1063/1.1674902.

29 A. V. Marenich, C. J. Cramer and D. G. Truhlar, Universal Solvation Model Based on Solute Electron Density and on A Continuum Model of the Solvent Defined by The Bulk Dielectric Constant and Atomic Surface Tensions, *J. Phys. Chem. B*, 2009, **113**, 6378–6396, DOI: 10.1021/jp810292n.

30 P. Winget, E. J. Weber, C. J. Cramer and D. G. Truhlar, Computational Electrochemistry: Aqueous One-Electron Oxidation Potentials for Substituted Anilines, *Phys. Chem. Chem. Phys.*, 2000, **2**, 1231–1239, DOI: 10.1039/A909076B.

31 P. Winget, C. J. Cramer and D. G. Truhlar, Computation of Equilibrium Oxidation and Reduction Potentials for Reversible and Dissociative Electron-Transfer Reactions in Solution, *Theor. Chem. Acc.*, 2004, **112**, 217–227, DOI: 10.1007/s00214-004-0577-0.

32 J. Zhang and T. Lu, Efficient Evaluation of Electrostatic Potential with Computerized Optimized Code, *Phys. Chem. Chem. Phys.*, 2021, **23**, 20323–20328, DOI: 10.1039/D1CP02805G.

33 T. Lu and F. Chen, Multiwfn: A Multifunctional Wavefunction Analyzer, *J. Comput. Chem.*, 2012, **33**, 580–592, DOI: 10.1002/jcc.22885.

34 W. Humphrey, A. Dalke and K. Schulten, VMD Visual Molecular Dynamics, *J. Mol. Graphics*, 1996, **14**, 33–38, DOI: 10.1016/0263-7855(96)00018-5.

35 L. Miao, L. Liu, K. Zhang and J. Chen, Molecular Design Strategy for High-Redox-Potential and Poorly Soluble N-Type Phenazine Derivatives as Cathode Materials for Lithium Batteries, *ChemSusChem*, 2020, **13**, 2337–2344, DOI: 10.1002/cssc.202000004.

36 J. Zhang and M. Dolg, ABCluster: The Artificial Bee Colony Algorithm for Cluster Global Optimization, *Phys. Chem. Chem. Phys.*, 2015, **17**, 24173–24181, DOI: 10.1039/C5CP04060D.

37 J. Zhang and M. Dolg, Global Optimization of Clusters of Rigid Molecules Using The Artificial Bee Colony Algorithm, *Phys. Chem. Chem. Phys.*, 2016, **18**, 3003–3010, DOI: 10.1039/C5CP06313B.

38 S. Grimme, J. Antony, S. Ehrlich and H. A. Krieg, Consistent and Accurate *Ab Initio* Parametrization of Density Functional Dispersion Correction (DFT-D) for The 94 Elements H-Pu, *J. Chem. Phys.*, 2010, **132**, 154104, DOI: 10.1063/1.3382344.

39 P. J. Stephens, F. J. Devlin, C. F. Chabalowski and M. J. Frisch, Ab Initio Calculation of Vibrational Absorption and Circular Dichroism Spectra Using Density Functional Force Fields, *J. Phys. Chem.*, 1994, **98**, 11623–11627, DOI: 10.1021/j100096a001.

40 M. M. Francl, W. J. Pietro, W. J. Hehre, J. S. Binkley, M. S. Gordon, D. J. DeFrees and J. A. Pople, Self-Consistent Molecular Orbital Methods. XXIII. A Polarization-Type Basis Set for Second-Row Elements, *J. Chem. Phys.*, 1982, **77**, 3654–3665, DOI: 10.1063/1.444267.

41 A. D. McLean and G. S. Chandler, Contracted Gaussian Basis Sets for Molecular Calculations. I. Second Row Atoms, Z = 11–18, *J. Chem. Phys.*, 2008, **72**, 5639–5648, DOI: 10.1063/1.438980.

42 G. W. Spitznagel, T. Clark, P. von Ragué Schleyer and W. J. Hehre, An Evaluation of the Performance of Diffuse Function-Augmented Basis Sets for Second Row Elements, Na-Cl, *J. Comput. Chem.*, 1987, **8**, 1109–1116, DOI: 10.1002/jcc.540080807.

43 J. Bergner, C. Walla, F. Rominger, A. Dreuw and M. Kivala, Inducing Curvature to Pyracylene upon π-Expansion, *Chem.–Eur. J.*, 2022, **28**, e202201554, DOI: 10.1002/chem.202201554.

44 R. Gu, Z. Ma, T. Cheng, Y. Lyu, A. Nie and B. Guo, Improved Electrochemical Performances of $LiCoO_2$ at Elevated Voltage

and Temperature with an *In Situ* Formed Spinel Coating Layer, *ACS Appl. Mater. Interfaces*, 2018, **10**, 31271–31279, DOI: 10.1021/acsami.8b08264.

45 M. M. Doeff, *Batteries: Overview of Battery Cathodes*; Lawrence Berkeley National Lab. (LBNL), Berkeley, CA, United States, 2010.

46 Y. Katsuyama, H. Kobayashi, K. Iwase, Y. Gambe and I. Honma, Are Redox-Active Organic Small Molecules Applicable for High-Voltage (>4 V) Lithium-Ion Battery Cathodes?, *Adv. Sci.*, 2022, **9**, 2200187, DOI: 10.1002/advs.202200187.

47 C. Peng, G.-H. Ning, J. Su, G. Zhong, W. Tang, B. Tian, C. Su, D. Yu, L. Zu, J. Yang, M.-F. Ng, Y.-S. Hu, Y. Yang, M. Armand and K. P. Loh, Reversible Multi-Electron Redox Chemistry of π-Conjugated N-Containing Heteroaromatic Molecule-Based Organic Cathodes, *Nat. Energy*, 2017, **2**, 17074, DOI: 10.1038/nenergy.2017.74.

48 M. S. Wu, N. T. H. Luu, T. H. Chen, H. Lyu, T. W. Huang, S. Dai, X. G. Sun, A. S. Ivanov, J. C. Lee, I. Popovs and W. Kaveevivitchai, Supramolecular Self-Assembled Multi-Electron-Acceptor Organic Molecule as High-Performance Cathode Material for Li-Ion Batteries, *Adv. Energy Mater.*, 2021, **11**, 2100330, DOI: 10.1002/aenm.202100330.

49 M. R. Tuttle, S. T. Davis and S. Zhang, Synergistic Effect of Hydrogen Bonding and π–π Stacking Enables Long Cycle Life in Organic Electrode Materials, *ACS Energy Lett.*, 2021, **6**, 643–649, DOI: 10.1021/acsenergylett.0c02604.

50 J. Lee and M. J. Park, Tattooing Dye as A Green Electrode Material for Lithium Batteries, *Adv. Energy Mater.*, 2017, **7**, 1602279, DOI: 10.1002/aenm.201602279.

51 P. F. Wang, H. Xin, T. T. Zuo, Q. Li, X. Yang, Y. X. Yin, X. Gao, X. Yu and Y. G. Guo, An Abnormal 3.7 Volt O3-Type Sodium-Ion Battery Cathode, *Angew. Chem., Int. Ed.*, 2018, **57**, 8178–8183, DOI: 10.1002/anie.201804130.

52 E. de la Llave, E. Talaie, E. Levi, P. K. Nayak, M. Dixit, P. T. Rao, P. Hartmann, F. Chesneau, D. T. Major, M. Greenstein, D. Aurbach and L. F. Nazar, Improving Energy Density and Structural Stability of Manganese Oxide Cathodes for Na-Ion Batteries by Structural Lithium Substitution, *Chem. Mater.*, 2016, **28**, 9064–9076, DOI: 10.1021/acs.chemmater.6b04078.

53 Y. Liu, X. Fang, A. Zhang, C. Shen, Q. Liu, H. A. Enaya and C. Zhou, Layered P2-$Na_{2/3}[Ni_{1/3}Mn_{2/3}]O_2$ as High-voltage Cathode for Sodium-ion Batteries: The Capacity Decay Mechanism and Al_2O_3 Surface Modification, *Nano Energy*, 2016, **27**, 27–34, DOI: 10.1016/j.nanoen.2016.06.026.

54 T. Song, W. Yao, P. Kiadkhunthod, Y. Zheng, N. Wu, X. Zhou, S. Tunmee, S. Sattayaporn and Y. Tang, A Low-Cost and Environmentally Friendly Mixed Polyanionic Cathode for Sodium-Ion Storage, *Angew. Chem.*, 2020, **132**, 750–755, DOI: 10.1002/ange.201912272.

55 N. Yabuuchi, M. Kajiyama, J. Iwatate, H. Nishikawa, S. Hitomi, R. Okuyama, R. Usui, Y. Yamada and S. Komaba, P2-type $Na_x[Fe_{1/2}Mn_{1/2}]O_2$ Made from Earth-abundant Elements for Rechargeable Na Batteries, *Nat. Mater.*, 2012, **11**, 512–517, DOI: 10.1038/nmat3309.

56 W. Li, C. Han, W. Wang, Q. Xia, S. Chou, Q. Gu, B. Johannessen, H. Liu and S. Dou, Stress Distortion Restraint to Boost the Sodium Ion Storage Performance of a Novel Binary Hexacyanoferrate, *Adv. Energy Mater.*, 2020, **10**, 1903006, DOI: 10.1002/aenm.201903006.

57 P. F. Wang, Y. You, Y. X. Yin, Y. S. Wang, L. J. Wan, L. Gu and Y. G. Guo, Suppressing the P2-O2 Phase Transition of $Na_{0.67}Mn_{0.67}Ni_{0.33}O_2$ by Magnesium Substitution for Improved Sodium-Ion Batteries, *Angew. Chem., Int. Ed.*, 2016, **55**, 7445–7449, DOI: 10.1002/ange.201602202.

58 P. Hu, C. Cai, X. Li, Z. Wei, M. Wang, C. Chen, T. Zhu, L. Mai and L. Zhou, V Doping in NASICON-Structured $Na_3MnTi(PO_4)_3$ Enables High-Energy and Stable Sodium Storage, *Adv. Funct. Mater.*, 2023, **34**, 2302045, DOI: 10.1002/adfm.202302045.

59 C. Fang, Y. Huang, L. Yuan, Y. Liu, W. Chen, Y. Huang, K. Chen, J. Han, Q. Liu and Y. Huang, A Metal-Organic Compound as Cathode Material with Super high Capacity Achieved by Reversible Cationic and Anionic Redox Chemistry for High-Energy Sodium-Ion Batteries, *Angew. Chem., Int. Ed.*, 2017, **56**, 6793–6797, DOI: 10.1002/ange.201701213.

60 H. Banda, D. Damien, K. Nagarajan, M. Hariharan and M. M. Shaijumon, A Polyimide Based All-organic Sodium Ion Battery, *J. Mater. Chem. A*, 2015, **3**, 10453, DOI: 10.1039/C5TA02043C.

61 Q. Zhao, W. Zhao, C. Zhang, Y. Wu, Q. Yuan, A. K. Whittaker and X. S. Zhao, Sodium-Ion Storage Mechanism in Triquinoxalinylene and a Strategy for Improving Electrode Stability, *Energy Fuels*, 2020, **34**, 5099–5105, DOI: 10.1021/acs.energyfuels.0c00798.

62 C. Huangfu, Z. Liu, X. Lu, Q. Liu, T. Wei and Z. Fan, Strong Oxidation Induced Quinone-rich Dopamine Polymerization onto Porous Carbons as Ultrahigh-capacity Organic Cathode for Sodium-ion Batteries, *Energy Storage Mater.*, 2021, **43**, 120–129, DOI: 10.1016/j.ensm.2021.08.043.

63 Y. Chen, Q. Zhu, K. Fan, Y. Gu, M. Sun, Z. Li, C. Zhang, Y. Wu, Q. Wang, S. Xu, J. Ma, C. Wang and W. Hu, Successive Storage of Cations and Anions by Ligands of π-d-Conjugated Coordination Polymers Enabling Robust Sodium-Ion Batteries, *Angew. Chem., Int. Ed.*, 2021, **60**, 18769–18776, DOI: 10.1002/anie.202106055.

64 X. Zhao, W. Qiu, C. Ma, Y. Zhao, K. Wang, W. Zhang, L. Kang and J. Liu, Superposed Redox Chemistry of Fused Carbon Rings in Cyclooctatetraene-Based Organic Molecules for High-Voltage and High-Capacity Cathodes, *ACS Appl. Mater. Interfaces*, 2018, **10**, 2496–2503, DOI: 10.1021/acsami.7b15495.

65 K. C. Kim, T. Liu, K. H. Jung, S. W. Lee and S. S. Jang, Unveiled Correlations between Electron Affinity and Solvation in Redox Potential of Quinone-based Sodium-ion Batteries, *Energy Storage Mater.*, 2019, **19**, 242–250, DOI: 10.1016/j.ensm.2019.01.017.

66 G. S. Jeong, K. H. Jung, S. Choi and K. C. Kim, Electrochemical Characteristics of Cyanoquinones as Organic Cathodes for High-Potential Sodium-Ion Batteries, *ACS Sustainable Chem. Eng.*, 2020, **8**, 11328–11336, DOI: 10.1021/acssuschemeng.0c03332.